IEEE Robotics and Automation Letters (RA-L) paper, presented at ICRA 2026, Vienna, Austria. Cite as RA-L paper.

Robust Admittance Control of an Electric Underwater Manipulator for Precise Motion and Safe Contact Inspection of Hydraulic Structures

Fei Wang[1], Haixin Liu[1], Lin Cao[1], Shitong Hou[2], Guangming Song[1], *Senior Member, IEEE*, and Aiguo Song[1], *Senior Member, IEEE*

***Abstract*—Inspection of hydraulic structures is crucial for ensuring the reliability and safety of infrastructures. Although underwater manipulators are essential tools, existing systems often lack sufficient compliance and safe interaction capabilities. This study develops a novel underwater manipulator system with a robust admittance control framework designed specifically for safe contact inspection tasks. The manipulator integrates a 6-axis force/torque sensor for contact force measurement and an ultrasonic detector for structural inspection. An underwater force estimation algorithm is implemented to ensure accurate force measurement under varying flow conditions. The proposed robust admittance control strategy comprises an inner-loop position controller, enhanced by an unknown system dynamics estimator and super-twisting sliding mode control, to counteract hydrodynamic disturbances and improve trajectory tracking accuracy. An outer-loop variable admittance controller, incorporating variable damping mechanism and adaptive feedback compensation, ensures compliant interactions and precise force control with minimal overshoot. Extensive experiments, including force measurement, motion and contact force control, and underwater thickness measurement, demonstrate the system's excellent performance, validating its effectiveness for hydraulic structure inspection tasks.**

***Index Terms*—Underwater manipulator, robust admittance control, contact inspection, hydraulic structure.**

I. Introduction

With the aging and increasing number of hydraulic infrastructures such as pipelines, bridges, and dams, underwater inspection and maintenance have become vital to ensure structural integrity and operational safety [1]. Currently, such tasks are primarily performed by human divers, who are limited to shallow water operations and exposed to safety hazards. As a result, there is growing demand for robotic systems to replace divers in hazardous or deep-water environments [2].

Manuscript received: July, 1, 2025; Revised September, 16, 2025; Accepted September, 27, 2025.

This paper was recommended for publication by Editor G. Loianno upon evaluation of the Associate Editor and Reviewers' comments. This work was supported by the National Natural Science Foundation of China under Grant 52127813 and Grant 62373098. (Corresponding author: Guangming Song.)

[1]Fei Wang, Haixin Liu, Lin Cao, Guangming Song, and Aiguo Song are with the State Key Laboratory of Digital Medical Engineering, Jiangsu Key Lab of Robot Sensing and Control, School of Instrument Science and Engineering, Southeast University, Nanjing 210096, China. (e-mail: neilwang@seu.edu.cn; lhaixin@seu.edu.cn; 220233619@seu.edu.cn; mikesong@seu.edu.cn; a.g.song@seu.edu.cn)

[2]Shitong Hou is with the National and Local Joint Engineering Research Center for Intelligent Construction and Maintenance, School of Civil Engineering, Southeast University, Nanjing 210096, China. (e-mail: shitonghou@seu.edu.cn)

Digital Object Identifier (DOI): see top of this page.

While remotely operated vehicles (ROVs) and autonomous underwater vehicles (AUVs) are widely used for visual inspections, they are inadequate for contact-based inspection or maintenance tasks that require physical interaction with structures. In such scenarios, underwater manipulators equipped with reliable control algorithms and specialized end-effectors provide a promising solution. These manipulators can be integrated into various robotic platforms, including underwater vehicle-manipulator systems (UVMSs) [3], [4], crawler-type robots [5], [6], and underwater legged robots (ULRs) [7], [8], enabling diverse contact operations. However, rigid manipulators controlled in position mode are prone to causing damage to target or themselves during interaction [9]. To ensure safe underwater inspection and maintenance of hydraulic infrastructures, compliance control is essential to regulate contact forces while protecting both the manipulator and the structure.

Physical demonstrations and applications of underwater robotic arms with compliance control remain limited. Patryk et al. [10] accomplished an adaptive admittance controller by modifying stiffness parameters for pipe inspections, although the system exhibited force overshoot and fluctuations. In [11], DexROV employed an admittance-based teleoperation system to perform intervention tasks in an oil-gas industry scenario. Shahab et al. [12] introduced a robust force-position controller for compliant contact with planar surfaces under hydrodynamic disturbances. In [13], a hybrid force-position control enhanced by sliding mode control (SMC) was tested on simplified targets without using a force/torque (F/T) sensor, showing effective contact force tracking but also inducing significant control noise and chattering. UTC-RS, an underwater robotic system, performs cleaning tasks on submerged planar structures by employing a hybrid force-position control [5].

Accurate trajectory tracking remains equally critical. Robust position control is required to guide the manipulator precisely from free motion to contact with submerged targets, particularly under hydrodynamic disturbances [14]. In [15], a SMC-based kinematic control scheme was proposed to maintain the fixed position for the manipulator of UVMS. Shang et al. [16] designed an adaptive control law based on neural network to identify underwater disturbance. While these methods improve motion control for underwater robots, they do not address contact forces. In [13], [17], SMC is combined with compliance control for force and position regulation under uncertainty, although chattering remained an issue.

Differing from the slow advancement on interaction tasks

IEEE Robotics and Automation Letters (RA-L) paper, presented at ICRA 2026, Vienna, Austria. Cite as RA-L paper.

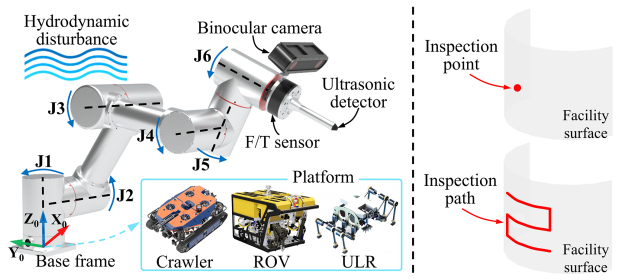

Fig. 1. Underwater manipulator system, adaptable to various underwater robotic platforms for point or path inspections of hydraulic structures.

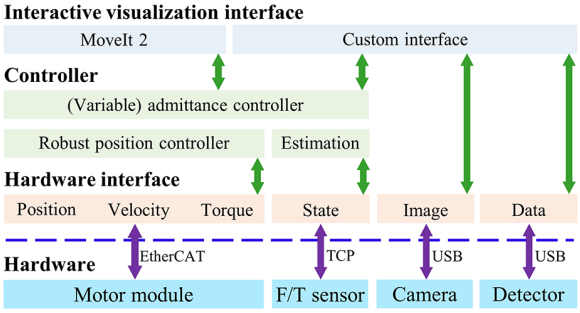

Fig. 2. ROS2-based control system.

with underwater manipulators, significant progress has been made in compliance control for industrial and collaborative robots [18]. A common approach is the online adaptation of control gains or impedance parameters [19], [20]. Uncertainty compensation and disturbance rejection methods have also rapidly advanced, such as the unknown system dynamics estimator (USDE) [21], [22] and super-twisting sliding mode control (ST SMC) [23], [24], which have enhanced precision and decreased chattering for robots under complex conditions. These improvements offer valuable insights into precise motion and safe interaction of underwater manipulators.

Despite the progress achieved, existing studies on underwater manipulators still face limitations such as unsatisfactory force control performance, static water experimental verification, and lack of real-world inspection data. Although adaptive compliance and robust motion control have advanced in industrial and collaborative robots, they remain underexplored in underwater applications, where hydrodynamic disturbances and unstructured environments impose additional challenges. To address these gaps, this article proposes a novel electric underwater manipulator system capable of robust trajectory tracking and compliant interaction for reliable contact inspection tasks. The key contributions are summarized as follows:

1) A reliable underwater manipulator system is developed, enabling accurate contact force measurement, precise motion control, and effective force regulation under varying water flow conditions.
2) A robust motion control algorithm integrating USDE and ST SMC is proposed, significantly improving trajectory tracking accuracy by compensating for hydrodynamic disturbances and model uncertainties.
3) A novel variable admittance controller with adaptive feedback compensation is developed, ensuring compliant interaction and precise force tracking with minimal overshoot and oscillations.

II. System Design and Challenges

A. Underwater Manipulator System

1) Mechanical structure: The overall structure of the developed underwater manipulator system is shown in Fig. 1. The electric manipulator features 6 degrees of freedom (6-DoF), enabling versatile poses for diverse underwater tasks. Detailed internal structures are provided in [25]. A binocular camera is mounted on the wrist for visual observation, while a 6-axis F/T sensor measures interaction forces during contact. The selected end-effector is an ultrasonic detector, which can be easily replaced with other probes for detecting corrosion, thickness, and other conditions of underwater structures. This manipulator system can be flexibly integrated onto various underwater robotic platforms (e.g., crawlers, ROVs, and ULRs) for inspection and maintenance. Contact inspection can be categorized into two modes: point inspection and continuous path inspection. Continuous path inspection, which moves the detector along the path to collect inspection data from multiple points, is an advanced form of point inspection.

2) ROS2-based Control System: The control system is implemented based on Robot Operating System 2 (ROS2), as illustrated in Fig. 2. ROS2 offers high real-time performance and strong scalability throughout the control process. The robust position controller and F/T estimation are implement via dedicated hardware interfaces. Further, the variable admittance controller and an interactive visualization interface are developed for robot control, image display, and inspection data storage. Due to the functionality and compatibility of ROS2, the developed system can integrate additional sensors and tools, supporting both teleoperation and autonomous operation for reliable underwater interventions.

Underwater robotic platforms equipped with manipulators typically operate in two distinct modes: fixed-base mode (used by crawlers, ULRs, or landed UVMS) and floating-base mode (used primarily by UVMS). The methods developed in this research exclusively focus on fixed-base configurations. Applying the proposed methods to floating-base platforms would require further analysis to address coupling effects from platform dynamics [4], [10], [11].

B. Challenges in Contact Inspection

Admittance control enables compliant behavior of the manipulator, emulating a mass-damper-spring system (see Fig. 3(a)). The inner-loop position controller tracks compliant position references $\boldsymbol{X}_c$ which are generated by the outloop admittance controller, as shown in Fig. 3(b). However, contact inspection using an underwater manipulator based on traditional admittance control face some challenges:

1) Contact force measurement: The accuracy of contact force measurements significantly affects both the safety and precision of inspections. However, force measurements $\hat{\boldsymbol{F}}_e$ are influenced by gravity, buoyancy, and zero drift caused by underwater conditions.

IEEE Robotics and Automation Letters (RA-L) paper, presented at ICRA 2026, Vienna, Austria. Cite as RA-L paper.

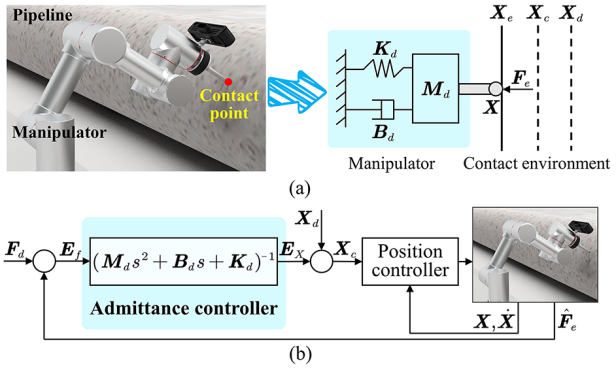

Fig. 3. Traditional admittance control. (a) System dynamics in contact with the external environment, (b) control schematic.

2) Inner-loop position controller: Underwater manipulators encounter hydrodynamic disturbances and model uncertainties compared to terrestrial robots. The dynamic model, combining disturbances and uncertainties into a unified disturbance torque $\boldsymbol{\tau}_{dist}$, is expressed as [13]:

$$\boldsymbol{M}(\boldsymbol{q})\ddot{\boldsymbol{q}}+\boldsymbol{C}(\boldsymbol{q},\dot{\boldsymbol{q}})\dot{\boldsymbol{q}}+\boldsymbol{D}(\boldsymbol{q},\dot{\boldsymbol{q}})\dot{\boldsymbol{q}}+\boldsymbol{G}(\boldsymbol{q}) = \boldsymbol{\tau}+\boldsymbol{\tau}_{dist}-\boldsymbol{J}^{\top}(\boldsymbol{q})\hat{\boldsymbol{F}}_e \tag{1}$$

where $\boldsymbol{q}, \dot{\boldsymbol{q}}, \ddot{\boldsymbol{q}} \in \mathbb{R}^n$ are joint positions, velocities, and accelerations. $\boldsymbol{M} \in \mathbb{R}^{n\times n}$ is the inertia matrix, $\boldsymbol{C} \in \mathbb{R}^{n\times n}$ is the Coriolis and centrifugal matrix, $\boldsymbol{D} \in \mathbb{R}^{n\times n}$ is the hydrodynamic drag force matrix, and $\boldsymbol{G} \in \mathbb{R}^n$ is the restoring force, accounting for the combined effects of gravity and buoyancy. $\boldsymbol{\tau} \in \mathbb{R}^n$ is the control torque. $\boldsymbol{J} \in \mathbb{R}^{n\times n}$ denotes Jacobian matrix. Then, the control torque is given by:

$$\boldsymbol{\tau} = \boldsymbol{M}\boldsymbol{u}_p + \boldsymbol{C}\dot{\boldsymbol{q}} + \boldsymbol{D}\dot{\boldsymbol{q}} + \boldsymbol{G} + \boldsymbol{J}^{\top}\hat{\boldsymbol{F}}_e - \boldsymbol{\tau}_{dist} \tag{2}$$

where $\boldsymbol{u}_p$ is position control law. When $\boldsymbol{u}_p$ is in the proportional-derivative (PD) form and $\boldsymbol{\tau}_{dist}$ is not estimated, (2) corresponds to computed torque control (CTC). Under hydrodynamic disturbances and model uncertainties, manipulators may significantly deviate from desired trajectory, risking inspection task failures and structural damage.

3) Out-loop admittance controller: Traditional admittance controller is given by:

$$\boldsymbol{M}_d\ddot{\boldsymbol{E}}_X + \boldsymbol{B}_d\dot{\boldsymbol{E}}_X + \boldsymbol{K}_d\boldsymbol{E}_X = -\boldsymbol{E}_f \tag{3}$$

where $\boldsymbol{M}_d$, $\boldsymbol{B}_d$, $\boldsymbol{K}_d \in \mathbb{R}^{n\times n}$ denote desired mass, damping, and stiffness matrices, respectively. $\boldsymbol{E}_X = \boldsymbol{X}_d - \boldsymbol{X}_c \in \mathbb{R}^n$ is the position correction between desired positions $\boldsymbol{X}_d$ and compliant positions $\boldsymbol{X}_c$. $\boldsymbol{F}_d$ denotes the desired contact force, and $\boldsymbol{E}_f = \boldsymbol{F}_d - \hat{\boldsymbol{F}}_e \in \mathbb{R}^n$. Traditional admittance control indirectly regulates interaction forces through desired impedance dynamics, relying on accurate environmental stiffness and position that are difficult to obtain in practice. This uncertainty often cause large force overshoot and poor force convergence, posing a critical limitation for underwater contact inspections.

Therefore, underwater force estimation and robust admittance control are developed to overcome challenges in accurate force measurement, precise trajectory tracking, and compliant force control, enabling safe and effective contact inspection of hydraulic structures using an underwater manipulator.

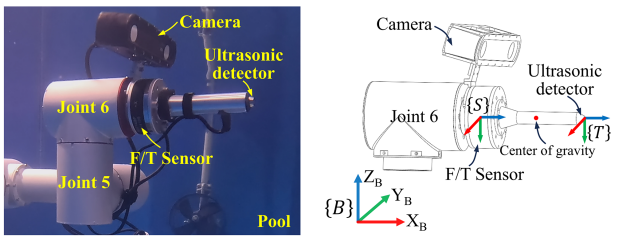

Fig. 4. Underwater F/T sensor. (a) Installation of the actual sensor, and (b) illustration of the coordinate systems for estimation and operation.

III. Underwater Force Estimation

The estimation is conducted underwater. Fig. 4 shows the F/T sensor installation and the corresponding coordinate systems, including the robot base frame $\{B\}$, sensor frame $\{S\}$, and tool frame $\{T\}$. The generic measurement vector $\boldsymbol{F}^S \in \mathbb{R}^6$ expressed in $\{S\}$ is

$$\boldsymbol{F}^S = \left[\boldsymbol{F}^S_{\text{tool}} + \boldsymbol{F}^S_{\text{off}} + \boldsymbol{F}^S_{\text{ext}}\right] = \begin{bmatrix}\boldsymbol{f}^S_{\text{tool}} + \boldsymbol{f}^S_{\text{off}} + \boldsymbol{f}^S_{\text{ext}} \\ \boldsymbol{\mu}^S_{\text{tool}} + \boldsymbol{\mu}^S_{\text{off}} + \boldsymbol{\mu}^S_{\text{ext}}\end{bmatrix} \tag{4}$$

where $\boldsymbol{F}^S_{\text{tool}}$ is the contribution of the end-effector, $\boldsymbol{F}^S_{\text{off}}$ is the offset, and $\boldsymbol{F}^S_{\text{ext}}$ represents the contact forces. $\boldsymbol{f}^S$, $\boldsymbol{\mu}^S \in \mathbb{R}^3$ are the force and torque measurements respectively.

The force and torque induced by the end-effector expressed in $\{S\}$ are

$$\boldsymbol{F}^S_{\text{tool}} = \begin{bmatrix}\boldsymbol{f}^S_{\text{tool}} \\ \boldsymbol{\mu}^S_{\text{tool}}\end{bmatrix} = \begin{bmatrix}\boldsymbol{R}^S_T\boldsymbol{R}^T_B(\boldsymbol{f}_g + \boldsymbol{f}_b) \\ \boldsymbol{R}^S_T\boldsymbol{R}^T_B(m\boldsymbol{r}_g - \rho V\boldsymbol{r}_b)\times\boldsymbol{g}\end{bmatrix} \tag{5}$$

where $\boldsymbol{R}^S_T$ is the rotation matrix between the $\{S\}$ and the $\{T\}$. The matrix $\boldsymbol{R}^T_B$ models the rotation between the $\{T\}$ and the $\{B\}$. The vectors $\boldsymbol{r}_g$ and $\boldsymbol{r}_b$ are the positions of the center of gravity and buoyancy of the end-effector. $\boldsymbol{f}_g = \begin{bmatrix}0 & 0 & mg_0\end{bmatrix}^{\top}$ and $\boldsymbol{f}_b = \begin{bmatrix}0 & 0 & -\rho V g_0\end{bmatrix}^{\top}$ are the weight and buoyancy of the end-effector, respectively, where m is the mass of the end-effector, g_0 is the gravity acceleration, ρ is the water density, V is the volume of fluid displaced by the end-effector, and $\boldsymbol{g} = \begin{bmatrix}0 & 0 & g_0\end{bmatrix}^{\top}$.

In order to identify the unknown parameters in (5) and $\boldsymbol{F}^S_{\text{off}}$, the measurements during estimation are expressed as

$$\begin{aligned}\begin{bmatrix}\boldsymbol{y}_1 \\ \boldsymbol{y}_2\end{bmatrix} &= \left[\boldsymbol{F}^S_{\text{tool}} + \boldsymbol{F}^S_{\text{off}}\right] = \begin{bmatrix}\boldsymbol{f}^S_{\text{tool}} + \boldsymbol{f}^S_{\text{off}} \\ \boldsymbol{\mu}^S_{\text{tool}} + \boldsymbol{\mu}^S_{\text{off}}\end{bmatrix} \\ &= \begin{bmatrix}\boldsymbol{R}^S_T\boldsymbol{R}^T_B(\boldsymbol{f}_g + \boldsymbol{f}_b) + \boldsymbol{f}^S_{\text{off}} \\ \boldsymbol{R}^S_T\boldsymbol{R}^T_B(m\boldsymbol{r}_g - \rho V\boldsymbol{r}_b)\times\boldsymbol{g} + \boldsymbol{\mu}^S_{\text{off}}\end{bmatrix}.\end{aligned} \tag{6}$$

$\boldsymbol{y}_1$ represents the force measurements, with its corresponding parameters to be estimated as follows:

$$\boldsymbol{\gamma}_1 = \begin{bmatrix}(m-\rho V) & \boldsymbol{f}^S_{\text{off}}\end{bmatrix}^{\top} \in \mathbb{R}^4. \tag{7}$$

The force measurement regressor composed of known quantities is defined as follows:

$$\begin{aligned}\boldsymbol{\Phi}_f &= \begin{bmatrix}\boldsymbol{\Gamma}_f & \boldsymbol{I}\end{bmatrix} \in \mathbb{R}^{3\times 4}, \\ \boldsymbol{\Gamma}_f &= \boldsymbol{R}^S_T\boldsymbol{R}^T_B \cdot \begin{bmatrix}0 & 0 & 1\end{bmatrix}^{\top} \in \mathbb{R}^3.\end{aligned} \tag{8}$$

IEEE Robotics and Automation Letters (RA-L) paper, presented at ICRA 2026, Vienna, Austria. Cite as RA-L paper.

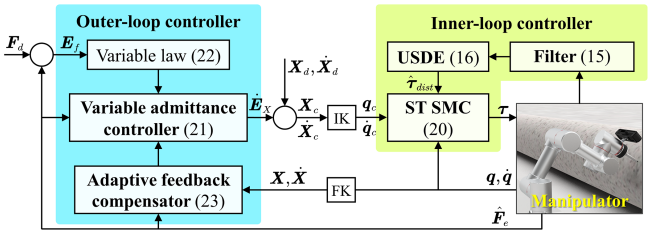

Fig. 5. Framework of the robust admittance control strategy, FK denotes forward kinematics, and IK denotes inverse kinematics.

The force measurements of (6) can be rewritten as follows:

$$\boldsymbol{y}_1 = \boldsymbol{\Phi}_f \boldsymbol{\gamma}_1. \tag{9}$$

Then, the unknown parameters $\boldsymbol{\gamma}_1$ can be computed using the least-squares regression method as:

$$\boldsymbol{\gamma}_1 = \boldsymbol{\Phi}_f^{\dagger} \boldsymbol{y}_1 \tag{10}$$

where $\boldsymbol{\Phi}_f^{\dagger}$ represents the pseudoinverse of $\boldsymbol{\Phi}_f$. $\boldsymbol{y}_2$ represents the torque measurements, with its corresponding parameters to be estimated as follows:

$$\boldsymbol{\gamma}_2 = \begin{bmatrix} (mg_0\boldsymbol{r}_g - \rho V g_0 \boldsymbol{r}_b) & \boldsymbol{\mu}_{off}^S \end{bmatrix}^\top \in \mathbb{R}^6, \tag{11}$$

whose regression process is identical to that of $\boldsymbol{\gamma}_1$. Then, the final vector encompassing all the parameters to be estimated can be obtained:

$$\begin{aligned} \boldsymbol{\gamma} &= \begin{bmatrix} \boldsymbol{\gamma}_1 & \boldsymbol{\gamma}_2 \end{bmatrix} \\ &= \begin{bmatrix} (m - \rho V) & \boldsymbol{f}_{off}^S & (mg_0\boldsymbol{r}_g - \rho V g_0 \boldsymbol{r}_b) & \boldsymbol{\mu}_{off}^S \end{bmatrix}^\top. \end{aligned} \tag{12}$$

Based on these calibrated parameters, $\boldsymbol{F}_{\text{ext}}^S$ can be obtained by removing $\boldsymbol{F}_{\text{tool}}^S$ and $\boldsymbol{F}_{\text{off}}^S$ from $\boldsymbol{F}^S$ in (4). Finally, rotating $\boldsymbol{F}_{\text{ext}}^S$ from the sensor frame $\{S\}$ to the robot base frame $\{B\}$,

$$\boldsymbol{F}_{\text{ext}}^B = \boldsymbol{R}_S^B \boldsymbol{F}_{\text{ext}}^S = \hat{\boldsymbol{F}}_e \ . \tag{13}$$

IV. Robust Admittance Control

A. USDE under Underwater Dynamics and Contact Forces

The original USDE [21] is modified by incorporating underwater dynamics and measured contact forces into the disturbance estimation, tailoring it for underwater contact inspection tasks. In system (1), the measured joint acceleration $\ddot{\boldsymbol{q}}$ is accompanied by significant noise, complicating accurate disturbance estimation. To circumvent the direct measurement of acceleration, auxiliary variables are introduced:

$$\begin{cases} \boldsymbol{P}(\boldsymbol{q}, \dot{\boldsymbol{q}}) = \boldsymbol{M}(\boldsymbol{q})\dot{\boldsymbol{q}} \\ \boldsymbol{H}(\boldsymbol{q}, \dot{\boldsymbol{q}}) = -\dot{\boldsymbol{M}}(\boldsymbol{q})\dot{\boldsymbol{q}} + \boldsymbol{C}(\boldsymbol{q}, \dot{\boldsymbol{q}})\dot{\boldsymbol{q}} + \boldsymbol{D}(\boldsymbol{q}, \dot{\boldsymbol{q}})\dot{\boldsymbol{q}} + \boldsymbol{G}(\boldsymbol{q}) \end{cases}$$

Thus, (1) can be rewritten as:

$$\dot{\boldsymbol{P}} + \boldsymbol{H} = \boldsymbol{\tau} + \boldsymbol{\tau}_{dist} - \boldsymbol{J}^\top \hat{\boldsymbol{F}}_e. \tag{14}$$

Since the term $\dot{\boldsymbol{P}}$ includes $\ddot{\boldsymbol{q}}$, several first-order filter operations are employed to avoid its direct computation:

$$\begin{cases} k\dot{\boldsymbol{P}}_f + \boldsymbol{P}_f = \boldsymbol{P}, & \boldsymbol{P}_f|_{t=0} = \boldsymbol{0} \\ k\dot{\boldsymbol{H}}_f + \boldsymbol{H}_f = \boldsymbol{H}, & \boldsymbol{H}_f|_{t=0} = \boldsymbol{0} \\ k\dot{\boldsymbol{\tau}}_f + \boldsymbol{\tau}_f = \boldsymbol{\tau}, & \boldsymbol{\tau}_f|_{t=0} = \boldsymbol{0} \\ k\dot{\hat{\boldsymbol{F}}}_{ef} + \hat{\boldsymbol{F}}_{ef} = \hat{\boldsymbol{F}}_e, & \hat{\boldsymbol{F}}_{ef}|_{t=0} = \boldsymbol{0} \end{cases} \tag{15}$$

where $k > 0$ is a scalar filter parameter, and $\boldsymbol{P}_f$, $\boldsymbol{H}_f$, $\boldsymbol{\tau}_f$, $\hat{\boldsymbol{F}}_{ef}$ represent filtered values of $\boldsymbol{P}$, $\boldsymbol{H}$, $\boldsymbol{\tau}$, and $\hat{\boldsymbol{F}}_e$, respectively. Substituting the filtered values into (14), the required disturbance estimation can be derived as:

$$\hat{\boldsymbol{\tau}}_{dist} = \frac{\boldsymbol{P} - \boldsymbol{P}_f}{k} + \boldsymbol{H}_f - \boldsymbol{\tau}_f + \boldsymbol{J}^\top \hat{\boldsymbol{F}}_{ef}. \tag{16}$$

B. Robust Position Controller Based on USDE and ST SMC

The proposed robust position controller, based on USDE and ST-SMC, is illustrated as the inner-loop component of the framework (see Fig. 5). The sliding manifold $\boldsymbol{S} \in \mathbb{R}^n$ is

$$\boldsymbol{S} = \dot{\boldsymbol{e}} + \boldsymbol{\eta}\boldsymbol{e} \tag{17}$$

where $\boldsymbol{\eta} \in \mathbb{R}^{n\times n}$ is a positive diagonal coefficient matrix, and $\boldsymbol{e} = \boldsymbol{q}_c - \boldsymbol{q}$ is the tracking error. When $\boldsymbol{S}$ converges to zero, $\boldsymbol{e}$ will converge to zero, ensuring precise trajectory tracking. The ST reaching law is designed as follows:

$$\dot{\boldsymbol{S}} = -\boldsymbol{T}_1 |\boldsymbol{S}|^{\frac{1}{2}} \text{sign}(\boldsymbol{S}) - \boldsymbol{T}_2 \int_0^T \text{sign}(\boldsymbol{S}) dt \tag{18}$$

where $\boldsymbol{T}_1$, $\boldsymbol{T}_2 \in \mathbb{R}^{n\times n}$ are positive diagonal control gain matrices, and T is the control cycle period. The resulting control law based on ST SMC is thus expressed as:

$$\boldsymbol{u}_p = \dot{\boldsymbol{\xi}} + \boldsymbol{T}_1 |\boldsymbol{S}|^{\frac{1}{2}} \text{sign}(\boldsymbol{S}) + \boldsymbol{T}_2 \int_0^T \text{sign}(\boldsymbol{S}) dt \tag{19}$$

with $\boldsymbol{\xi} = \dot{\boldsymbol{q}}_c + \boldsymbol{\eta}\boldsymbol{e}$ being an intermediate variable. Consequently, the control torque based on USDE and ST SMC is

$$\begin{aligned} \boldsymbol{\tau} =& \boldsymbol{T}_1 |\boldsymbol{S}|^{\frac{1}{2}} \text{sign}(\boldsymbol{S}) + \boldsymbol{T}_2 \int_0^T \text{sign}(\boldsymbol{S}) dt + \boldsymbol{M}\dot{\boldsymbol{\xi}} \\ &+ \boldsymbol{C}\dot{\boldsymbol{q}} + \boldsymbol{D}\dot{\boldsymbol{q}} + \boldsymbol{G} + \boldsymbol{J}^\top \hat{\boldsymbol{F}}_e - \hat{\boldsymbol{\tau}}_{dist}. \end{aligned} \tag{20}$$

In this control framework, the USDE effectively compensates major disturbances and uncertainties, enhancing system robustness. Meanwhile, the ST SMC method further corrects residual tracking errors, maintaining precise motion tracking with low control gains and minimizing torque chattering.

C. Variable Admittance Controller with Adaptive Feedback Compensator

A novel variable admittance control method incorporating an adaptive feedback compensator is proposed, as illustrated by the outer-loop controller in Fig. 5. In this scheme, the variable admittance controller enables effective contact force tracking, while adaptive feedback contributes to stabilizing the contact force.

The proposed variable admittance controller combined with adaptive feedback compensation is formulated as:

$$\underbrace{\boldsymbol{M}_d \ddot{\boldsymbol{E}}_X + \hat{\boldsymbol{B}} \dot{\boldsymbol{E}}_X}_{variable\ admittance} + \underbrace{\delta \hat{\boldsymbol{F}}}_{adaptive} = \hat{\boldsymbol{F}}_e \tag{21}$$

where $\hat{\boldsymbol{B}}$ is the variable damping matrix adaptively tuned based on the contact force error. It is defined as:

$$\hat{\boldsymbol{B}} = \boldsymbol{B}_d + \frac{\left(\boldsymbol{K}_p \boldsymbol{E}_f + \boldsymbol{K}_v \dot{\boldsymbol{E}}_f\right)}{\dot{\boldsymbol{E}}_X} \tag{22}$$

IEEE Robotics and Automation Letters (RA-L) paper, presented at ICRA 2026, Vienna, Austria. Cite as RA-L paper.

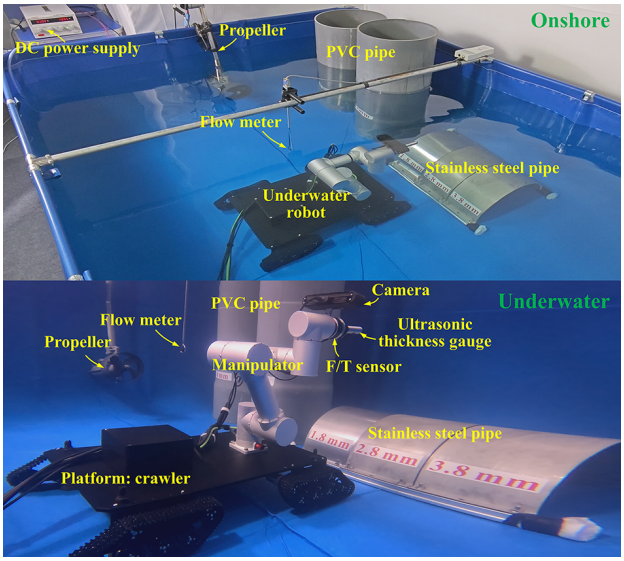

Fig. 6. Experimental setup for validating the developed system.

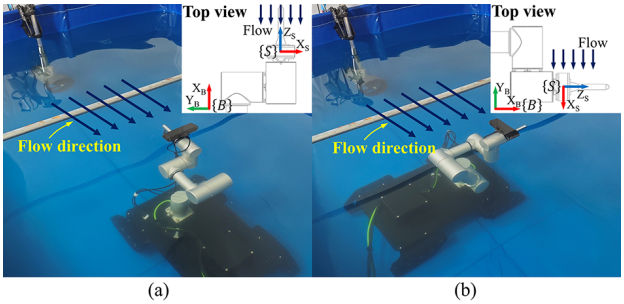

Fig. 7. Flow impact on the F/T measurements in two directions: (a) along $-z$ of $\{S\}$, and (b) along $+x$ of $\{S\}$.

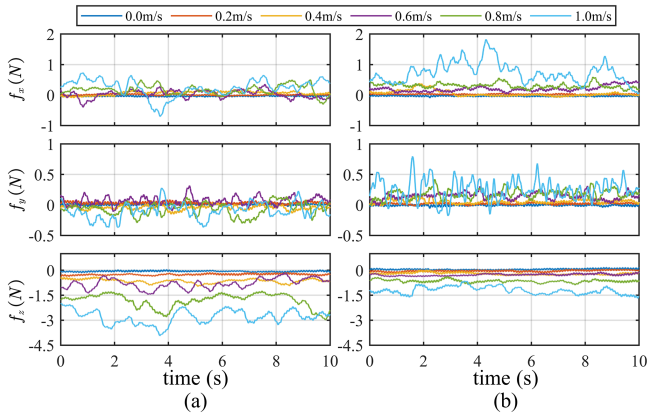

Fig. 8. Force values at different flow velocities using 0.0 m/s flow estimation parameters: (a) along $-z$ of $\{S\}$, and (b) along $+x$ of $\{S\}$.

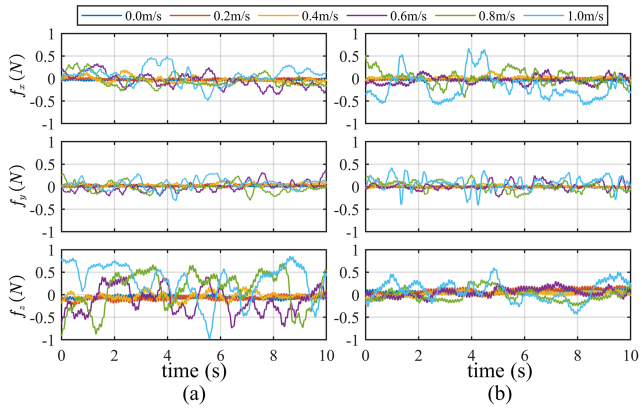

Fig. 9. Force values after estimation at different flow velocities: (a) along $-z$ of $\{S\}$, and (b) along $+x$ of $\{S\}$.

where $\boldsymbol{K}_p$ and $\boldsymbol{K}_v$ are diagonal positive-definite gain matrices. Unlike traditional admittance controller, the proposed method excludes the stiffness term, reducing system complexity and enhancing system stability [19], and adjusts damping parameters based on contact force error to correct inner-loop position control inputs, ultimately achieving force tracking.

The adaptive feedback compensator, defined as $\delta\hat{\boldsymbol{F}}$, aims to alleviate impacts during the initial contact transition and regulate uncertain interaction forces during continuous contact. This adaptive item is proportional to the end-effector velocity and the measured contact force:

$$\delta\hat{\boldsymbol{F}} = \hat{\boldsymbol{\lambda}}(t) \odot \dot{\boldsymbol{X}} \tag{23}$$

where $\hat{\boldsymbol{\lambda}}(t)$ is the adaptive control gain updated online according to the magnitude of the contact force, given as:

$$\hat{\boldsymbol{\lambda}}(t) = \beta|\hat{\boldsymbol{F}}_e| \geq 0 \tag{24}$$

with β being a positive scalar gain. Specifically, prior to contact ($|\hat{\boldsymbol{F}}_e| = 0$), the adaptive term (23) remains inactive irrespective of end-effector velocity. Once contact is established ($|\hat{\boldsymbol{F}}_e| \neq 0$), two scenarios arises:

1) Initial contact transition: during the transition from free motion to contact, both the contact force and end-effector velocity are relatively high. The resulting large adaptive term stabilizes the manipulator motion, thereby reducing impact and limiting force overshoot.
2) Continuous stable contact: the end-effector moves at low velocities, producing a smaller adaptive term that smooths force fluctuations. In this condition, the variable admittance controller dominates, ensuring precise force convergence with minimal oscillations.

V. Experiments and Results

A. Experimental Setup

The experiments were conducted in a 3m×2.5m×1.2m water tank, and the setup is depicted in Fig. 6. The designed underwater manipulator [25], with a waterproof rating of 300 m, a repeatability of ±0.05 mm, a weight of 10.2 kg, and a payload capacity of 7 kg, is mounted on a crawler platform to perform the inspection tasks. A waterproofed ZED 2i stereo camera and a 6-axis F/T sensor M3714BP from Sunrise Instruments are installed on the wrist of manipulator. An ultrasonic thickness gauge is selected as the detector to measure the thickness of hydraulic structures. These devices are connected to an onshore control computer running with Ubuntu 22.04 LTS (real-time kernel, Linux 6.2.0-rt3) and ROS2 Humble. The inspection targets consists of commonly

IEEE Robotics and Automation Letters (RA-L) paper, presented at ICRA 2026, Vienna, Austria. Cite as RA-L paper.

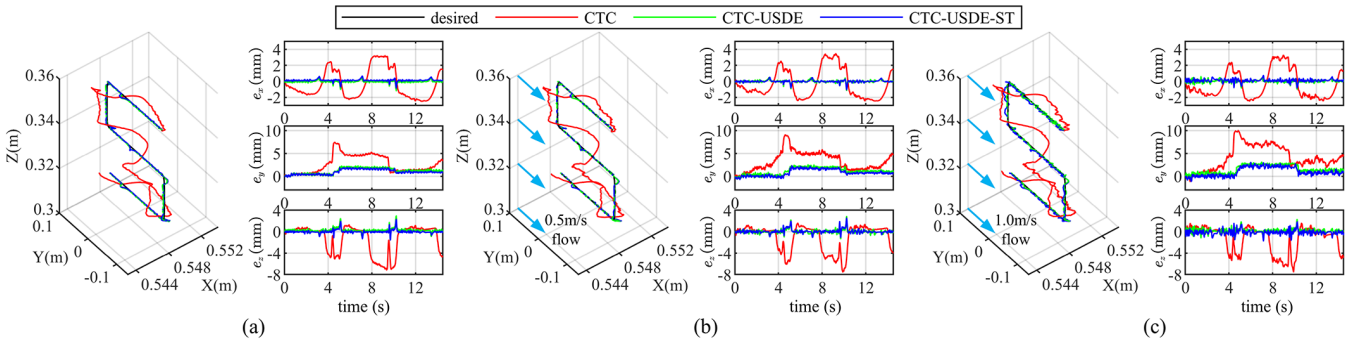

Fig. 10. Performance comparison of different position controllers at varying flow velocities: (a) 0.0m/s, (b) 0.5m/s, and (c) 1.0m/s. The Cartesian trajectories and errors represent the motion of end-effector in the $\{B\}$ frame, with the water flow directed along the negative y-axis.

used stainless steel and PVC pipes in hydraulic structures, each with a diameter of 40 cm. The stainless steel pipes are available in three thicknesses: 1.8 mm, 2.8 mm, and 3.8 mm, while the PVC pipes have two thicknesses: 6 mm and 9 mm. To evaluate performance under different water flow velocities, an adjustable-speed propeller is used to generate various stable flow conditions, and a flow meter is employed to measure the water velocity in the operating area.

B. Force Measurement Experiments

The manipulator is placed in two different postures (see Fig. 7) to investigate the impact of varying flow velocities and directions on the F/T sensor measurements. When flow is applied along the negative z-axis ($-z$) of $\{S\}$, increasing flow velocity induces a notable offset in f_z and amplifies fluctuations (see Fig. 8(a)). f_x and f_y also exhibit increased fluctuations, although they remain centered around zero. Under flow along the positive x-axis ($+x$) of $\{S\}$, f_x shows an increasing offset and fluctuation amplitude with rising velocity (see Fig. 8(b)). The observed f_x offset is smaller than the f_z offset in the prior configuration, due to the reduced hydrodynamic profile of the end-effector along the x-axis. In this posture, f_y is no longer symmetric about zero, and f_z increases due to cross-axis forces. After applying the designed estimation method, force measurements across all flow directions and velocities converge around zero with substantially reduced bias, as shown in Fig. 9, demonstrating the robustness and effectiveness of the estimation. For instance, under 1.0 m/s flow along $-z$, the fluctuation range of f_z is constrained within ± 1.0 N, while for flow along $+x$, f_x fluctuates within ± 0.6 N. Measurements on other axes also fluctuate but not as significantly as those in the direction of flow, remaining within a smaller range.

C. Trajectory Tracking Experiments in Free Space

Fig. 10 illustrates the trajectory tracking performance of three position controllers—CTC (2), CTC-USDE, and the proposed CTC-USDE-ST (20)—under different water flow velocities. The filter coefficient is set to $k = 0.05$. The control gains, initially selected with reference to [23], [24] and subsequently fine-tuned through experimental validation, are configured as

TABLE I
TRAJECTORY TRACKING PERFORMANCE

		CTC	CTC-USDE	CTC-USDE-ST
0.0 m/s	RMSE (mm)	4.7612	1.4168	1.1700
	Improvement	0	70.2%	75.4%
0.5 m/s	RMSE (mm)	5.0033	1.5043	1.2501
	Improvement	0	69.9%	75.0%
1.0 m/s	RMSE (mm)	5.9256	1.8161	1.4906
	Improvement	0	69.3%	74.8%

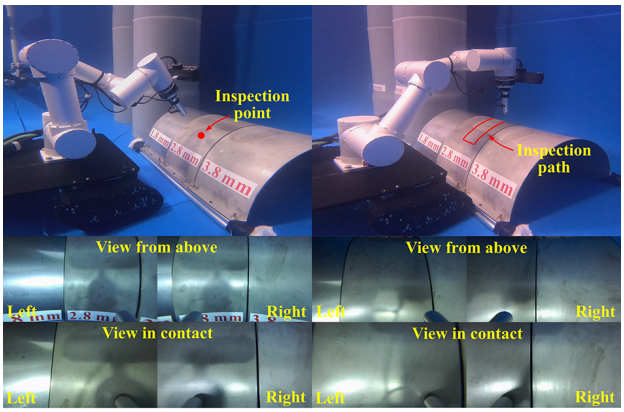

Fig. 11. Scenarios of (a) point inspection and (b) continuous path inspection along with the corresponding views from the stereo camera.

$\boldsymbol{\eta} = \text{diag}([8\ 8\ 8\ 8\ 8\ 8])$, $\boldsymbol{T}_1 = \text{diag}([2\ 2\ 2\ 1\ 1\ 1])$, and $\boldsymbol{T}_2 = \text{diag}([6\ 6\ 6\ 2\ 2\ 2])$.

The baseline CTC, lacking estimation and compensation for model uncertainties and hydrodynamic disturbances, exhibits significant trajectory deviation. In contrast, CTC-USDE markedly enhances tracking accuracy by estimating disturbances. The integration of ST SMC in CTC-USDE-ST further reduces position errors and improves system robustness. Notably, as flow velocity increases, trajectory fluctuations and errors intensify, particularly in e_y component due to the flow acting along the negative y-axis of $\{B\}$. To quantitatively assess controller performance, the root-mean-square error (RMSE) is computed under each flow condition, as summarized in Table I. The USDE module enables effective disturbance estimation, leading to substantial accuracy gains

IEEE Robotics and Automation Letters (RA-L) paper, presented at ICRA 2026, Vienna, Austria. Cite as RA-L paper.

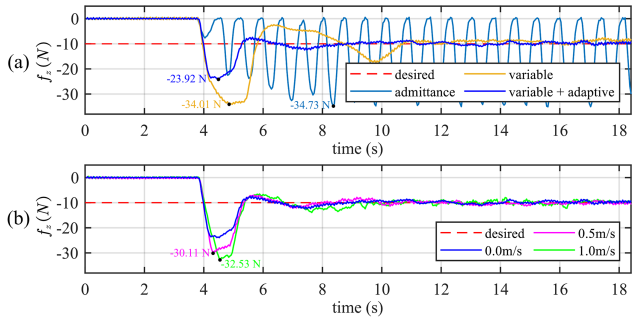

Fig. 12. Comparison of contact forces during point inspection: (a) f_z at 0.0 m/s flow using different force control strategies; (b) f_z at different flow velocities using the proposed controller.

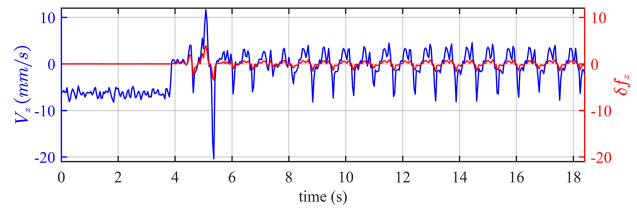

Fig. 13. Variations of the z-axis velocity and adaptive term during point inspection at 0.0 m/s flow velocity using the proposed controller.

over the baseline. The proposed method, based on USDE and ST SMC, achieves the lowest RMSE across all cases. At 1.0 m/s flow, the RMSE is reduced to 1.4906 mm, representing a 74.8% improvement compared to CTC, thereby validating the superior robustness and precision of the proposed controller under strong disturbances.

D. Contact and Inspection Experiments

Two inspection modes are evaluated for pipe thickness measurement: point inspection and continuous path inspection, as shown in Fig. 11. The admittance parameters, initially selected with reference to [10], [19] and subsequently fine-tuned through experimental trials, are set to $\boldsymbol{M}_d = \mathrm{diag}([10, 10, 10, 1, 1, 1])$, $\boldsymbol{B}_d = \mathrm{diag}([400, 400, 400, 40, 40, 40])$, and $\boldsymbol{K}_d = \mathrm{diag}([1000, 1000, 1000, 100, 100, 100])$. Variable damping control gains are configured as $\boldsymbol{K}_p = 120\boldsymbol{I}$ and $\boldsymbol{K}_v = 10\boldsymbol{I}$. The z-axis controller tracks a desired contact force of 10 N, while conventional admittance control is used on other axes.

Point Inspection: Fig. 12(a) shows that traditional admittance control fails to regulate contact force, leading to large oscillations up to -34.73 N. In contrast, the proposed controller suppresses oscillations and overshoot (peak force -23.92 N) and converges to the desired force within approximately 4 s. Fig. 13 illustrates the adaptive term's response to velocity variations: it remains zero before contact, increases during transition, and stabilizes in steady contact, effectively reducing overshoot and improving convergence. The fluctuation of the z-axis velocity observed after 6 s arises from the adaptive adjustment process, where the controller continuously modifies its output based on contact force errors to maintain the desired force. As shown in Fig. 12(b), higher flow velocities increase

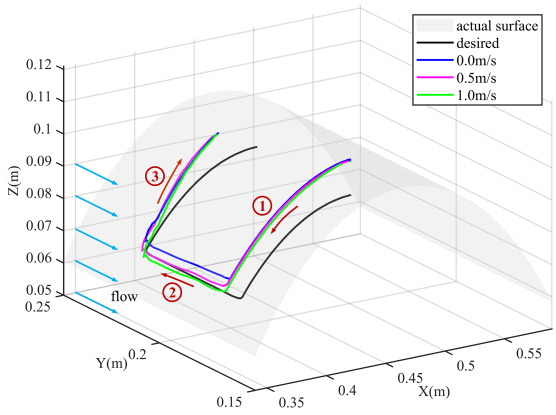

Fig. 14. Trajectories during continuous path inspection using the proposed controller at different flow velocities.

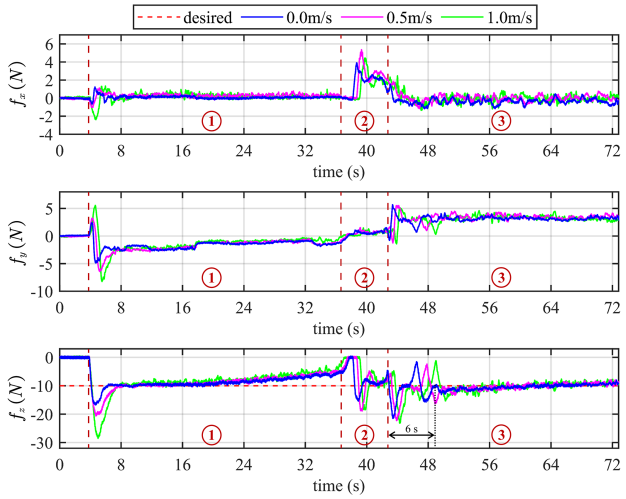

Fig. 15. Comparison of contact forces during continuous path inspection using the proposed controller at different flow velocities.

force overshoot and convergence time. Nevertheless, the proposed controller maintains accurate z-axis force tracking.

Continuous Path Inspection: Fig. 14 depicts the inspection trajectory across three segments on the pipe surface, while Fig. 15 presents corresponding force profiles. At the start of contact, f_z rapidly approaches the desired value. However, during trajectory execution, dynamic position errors and frictional forces degrade performance, especially in the second segment, where f_z fluctuations reach approximately -20 N. Changing travel direction reverses f_y and induces noticeable fluctuations of about -22 N in f_z at the beginning of the third segment. This phenomenon is attributed to cumulative motion errors arising from continuous controller adjustments of the desired position, deviations induced by contact friction, and changes in the contact state during the transition to the third segment. Potential mitigation could be achieved through online error compensation or vision-based accurate path planning. After roughly 6 s of adjustment, f_z converges to the desired value and remains stable. Despite increased fluctuations under higher flow rates, force tracking remains robust.

Thickness Measurement Accuracy: In point inspection mode, each pipe is measured 10 times, while in continuous

IEEE Robotics and Automation Letters (RA-L) paper, presented at ICRA 2026, Vienna, Austria. Cite as RA-L paper.

TABLE II
PIPE THICKNESS INSPECTION AT 0.5 M/S WATER FLOW

		Stainless steel pipe (mm)			PVC pipe (mm)	
Nominal thickness		1.8	2.8	3.8	6.0	9.0
Actual thickness		1.81	2.84	3.84	6.05	9.12
Point	Min	1.81	2.82	3.86	6.03	9.09
	Max	1.91	2.93	3.96	6.15	9.23
	Average	1.848	2.852	3.894	6.096	9.156
Path	Min	1.73	2.77	3.80	6.01	9.05
	Max	1.95	3.04	4.06	6.29	9.30
	Average	1.836	2.847	3.919	6.113	9.186

path inspection, data are collected every 3 s, yielding 18 valid measurements. Table II presents the statistical results of the pipe thickness measurements under both inspection modes at a 0.5 m/s water flow. Point inspection mode yields smaller variances between minimum and maximum values, reflecting higher precision. While continuous path inspection mode introduces slightly larger deviations due to motion-induced disturbances, it remains accurate and efficient for practical use. Comparable performance across all pipe materials and thicknesses confirms the system's reliability and adaptability for underwater non-destructive inspection.

VI. CONCLUSION

This study presents a robust underwater manipulator system tailored for safe and precise contact inspection of hydraulic structures. The 6-DoF electric manipulator integrates a 6-axis F/T sensor, a stereo camera, and an ultrasonic thickness gauge to support visual perception, force sensing, and non-destructive inspection. To precisely measure contact forces, an estimation algorithm for F/T sensor is developed. Building on this, a robust admittance control framework is proposed, comprising an inner-loop robust position controller and an outer-loop variable admittance controller. This controller enables reliable trajectory tracking and compliant force regulation, even in dynamic underwater environments. These advancements facilitate inspection of hydraulic structures, such as pipe thickness measurements. Future work will focus on (i) integrating alternative end-effectors such as rotary brushes or corrosion probes, and (ii) deploying the system on in-situ hydraulic facilities to validate long-term performance and durability.

REFERENCES

[1] F. Nauert and P. Kampmann, "Inspection and maintenance of industrial infrastructure with autonomous underwater robots," *Front. Robot. AI*, vol. 10, 2023.

[2] P. Ridao, M. Carreras, D. Ribas, P. J. Sanz, and G. Oliver, "Intervention auvs: the next challenge," *Annu. Rev. Control*, vol. 40, pp. 227–241, 2015.

[3] M. Cai, Y. Wang, S. Wang, R. Wang, and M. Tan, "Autonomous manipulation of an underwater vehicle-manipulator system by a composite control scheme with disturbance estimation," *IEEE Trans. Autom. Sci. Eng.*, vol. 21, no. 1, pp. 1012–1022, 2024.

[4] E. Simetti, R. Campos, D. Di Vito, J. Quintana, G. Antonelli, R. Garcia, and A. Turetta, "Sea mining exploration with an uvms: Experimental validation of the control and perception framework," *IEEE/ASME Trans. Mechatronics*, vol. 26, no. 3, pp. 1635–1645, 2020.

[5] J. Mao, J. Zhou, F. Xie, Y. Liu, G. Song, and A. Song, "UTC-RS: An underwater tracked cleaning robot system for hydraulic structures," *IEEE Robot. Automat. Lett.*, vol. 10, no. 3, pp. 2311–2318, 2025.

[6] L. Chen, R. Cui, W. Yan, H. Xu, H. Zhao, and H. Li, "Design and climbing control of an underwater robot for ship hull cleaning," *Ocean Eng.*, vol. 274, p. 114024, 2023.

[7] G. Picardi, M. Chellapurath, S. Iacoponi, S. Stefanni, C. Laschi, and M. Calisti, "Bioinspired underwater legged robot for seabed exploration with low environmental disturbance," *Sci. Robot.*, vol. 5, no. 42, p. eaaz1012, 2020.

[8] A. Astolfi, M. Chellapurath, G. Picardi, M. Capriotti, K. Mladinich, C. Laschi, S. Stefanni, and M. Calisti, "Marine sediment sampling with an underwater legged robot: A user-driven sampling approach for microplastic analysis," *IEEE Robot. Autom. Mag.*, vol. 31, no. 1, pp. 62–71, 2024.

[9] E. Simetti, F. Wanderlingh, S. Torelli, M. Bibuli, A. Odetti, G. Bruzzone, D. L. Rizzini, J. Aleotti, G. Palli, L. Moriello, and U. Scarcia, "Autonomous underwater intervention: Experimental results of the maris project," *IEEE J. Ocean. Eng.*, vol. 43, no. 3, pp. 620–639, 2018.

[10] P. Cieślak and P. Ridao, "Adaptive admittance control in task-priority framework for contact force control in autonomous underwater floating manipulation," in *Proc. IEEE/RSJ Int. Conf. Intell. Robots Syst. (IROS)*, 2018, pp. 6646–6651.

[11] P. Di Lillo, E. Simetti, F. Wanderlingh, G. Casalino, and G. Antonelli, "Underwater intervention with remote supervision via satellite communication: Developed control architecture and experimental results within the dexrov project," *IEEE Trans. Control Syst. Technol.*, vol. 29, no. 1, pp. 108–123, 2020.

[12] S. Heshmati-Alamdari, C. P. Bechlioulis, G. C. Karras, A. Nikou, D. V. Dimarogonas, and K. J. Kyriakopoulos, "A robust interaction control approach for underwater vehicle manipulator systems," *Annu. Rev. Control*, vol. 46, pp. 315–325, 2018.

[13] C. Barbalata, M. W. Dunnigan, and Y. Petillot, "Position/force operational space control for underwater manipulation," *Robot. Auto. Syst.*, vol. 100, pp. 150–159, 2018.

[14] R. Gabl, T. Davey, Y. Cao, Q. Li, B. Li, K. L. Walker, F. Giorgio-Serchi, S. Aracri, A. Kiprakis, A. A. Stokes, and D. M. Ingram, "Hydrodynamic loads on a restrained rov under waves and current," *Ocean Eng.*, vol. 234, p. 109279, 2021.

[15] B. O. A. Haugaløkken, E. K. Jørgensen, and I. Schjølberg, "Experimental validation of end-effector stabilization for underwater vehicle-manipulator systems in subsea operations," *Robot. Auto. Syst.*, vol. 109, pp. 1–12, 2018.

[16] D. Shang, X. Li, M. Yin, and S. Zhou, "Rotation tracking control strategy of underwater flexible telescopic manipulator based on neural network compensation for water environment disturbance," *Ocean Eng.*, vol. 284, p. 115245, 2023.

[17] P. Dai, W. Lu, K. Le, and D. Liu, "Sliding mode impedance control for contact intervention of an i-auv: Simulation and experimental validation," *Ocean Eng.*, vol. 196, p. 106855, 2020.

[18] M. Suomalainen, Y. Karayiannidis, and V. Kyrki, "A survey of robot manipulation in contact," *Robot. Auto. Syst.*, vol. 156, p. 104224, 2022.

[19] J. Duan, Y. Gan, M. Chen, and X. Dai, "Adaptive variable impedance control for dynamic contact force tracking in uncertain environment," *Robot. Auto. Syst.*, vol. 102, pp. 54–65, 2018.

[20] Y. Michel, M. Saveriano, and D. Lee, "A passivity-based approach for variable stiffness control with dynamical systems," *IEEE Trans. Autom. Sci. Eng.*, vol. 21, no. 4, pp. 6265–6276, 2024.

[21] J. Na, B. Jing, Y. Huang, G. Gao, and C. Zhang, "Unknown system dynamics estimator for motion control of nonlinear robotic systems," *IEEE Trans. Ind. Electron.*, vol. 67, no. 5, pp. 3850–3859, 2020.

[22] B. Jing, J. Na, H. Duan, X. Wang, and Y. Huang, "A usde-based control for bilateral teleoperation systems with time-varying delays," *IEEE Trans. Autom. Sci. Eng.*, pp. 1–11, 2024.

[23] A. Chalanga, S. Kamal, L. M. Fridman, B. Bandyopadhyay, and J. A. Moreno, "Implementation of super-twisting control: Super-twisting and higher order sliding-mode observer-based approaches," *IEEE Trans. Ind. Electron.*, vol. 63, no. 6, pp. 3677–3685, 2016.

[24] S. Zhang, S. Cheng, and Z. Jin, "Variable trajectory impedance: A super-twisting sliding mode control method for mobile manipulator based on identification model," *IEEE Trans. Ind. Electron.*, pp. 1–10, 2024.

[25] F. Wang, H. Liu, L. Cao, F. Xie, G. Song, and A. Song, "A novel lightweight underwater manipulator based on ros2 for reliable intervention," in *Proc. Int. Conf. Autom., Control Robot. Eng. (CACRE)*, 2024, pp. 345–349.